

Electronic correlations and transport in iron at Earth's core conditions

L. V. Pourovskii,^{1,2} J. Mravlje,³ M. Pozzo,⁴ and D. Alfè^{4,5}

¹*CPHT, CNRS, Ecole Polytechnique, Institut Polytechnique de Paris, F-91128 Palaiseau, France*

²*Collège de France, 11 place Marcelin Berthelot, 75005 Paris, France*

³*Josef Stefan Institute, SI-1000, Ljubljana, Slovenija*

⁴*Department of Earth Sciences and London Centre for Nanotechnology,*

University College London, Gower Street, London WC1E 6BT, United Kingdom

⁵*Dipartimento di Fisica Ettore Pancini, Università di Napoli Federico II, Monte S. Angelo, I-80126 Napoli, Italy.*

(Dated: December 22, 2024)

The transport properties of iron under inner core conditions are essential input for the geophysical modeling of the Earth's interior but are poorly constrained experimentally. We calculate the electrical and thermal conductivities of iron at Earth's inner core conditions taking into account consistently the thermal disorder due to the motion of ions and the electronic correlations. We focus mainly on the body-centered cubic (bcc) phase predicted to be stable at the core's conditions by several recent works. The total calculated thermal conductivity is 220 W/(m·K) including both the electron-electron scattering (EES) and electron-lattice scattering (ELS), with the EES contribution of about 20%. Thermal disorder is found to suppress the non-Fermi-liquid behavior characteristic for the perfect bcc iron and thus to reduce the EES. The total conductivity exhibits a markedly weaker sensitivity to increase of the EES as compared to the Matthiessen's rule, hence, the electron-lattice and electron-electron contributions are intertwined and cannot be treated separately. We also calculate the conductivity in the hexagonal close packed (hcp) iron phase, and again find the EES is not increased by the thermal disorder and is found to be weak there, too. Our main finding of a relatively weak EES thus holds for the both likely iron phases at Earth's core conditions.

Knowing the transport properties of iron at high-pressure and high-temperature conditions relevant to the Earth's core is essential for modeling the Earth's geodynamo mechanism that maintains the Earth's magnetic field.¹ The key quantity is the thermal conductivity that needs to be low enough for the transfer of heat in the liquid outer core to proceed by a convective mechanism.² Whereas quite low values of thermal conductivity were assumed (based on extrapolation of low-temperature data to higher temperatures) for a long time^{3,4} recent first principle calculations^{5,6} reported higher values.

These results have important implications. If the thermal conductivity is high, convection can be sustained only by a large heat flow⁴ associated with a younger Earth's inner core (some evidence for the latter was recently reported⁷). The thermal conductivity of solid iron is a key input for models of the inner core's anisotropy;^{8–10} a rather high conductivity have been recently predicted for hexagonal close-packed (hcp) ϵ -Fe at the relevant conditions.^{11,12} Experimentally, reaching high-temperatures and high-pressures is challenging and there is large scatter in the data from direct measurements.^{13–15} The transport properties are not the only ones to be determined with poor confidence: whereas the main constituent of the solid inner core is usually assumed to be the hcp ϵ -phase some experiments show evidence of the bcc phase.^{16,17} bcc-Fe was also predicted to be the stable phase of iron at inner-core conditions by recent molecular dynamics simulations.¹⁸

From the theoretical side the transport mechanisms in iron at Earth's core conditions are also incompletely understood with several important fundamental questions not resolved to date: (i) whereas and to what extent the

electronic correlations affect the transport properties is being intensely debated,^{12,19–21} (ii) the question of the interplay of the EES and electron-lattice scattering (ELS), namely: Is the Mathiessen's rule that estimates the total scattering rate from the sum of the individual ones valid? (iii) Does the Wiedemann-Franz law that relates the thermal and electrical conductivity apply? For correlated metals in a Fermi liquid regime the proportionality constant (the Lorenz number) is greatly affected by the energy dependence of the corresponding inelastic scattering rate.¹²

For crystalline hcp Fe Pourovskii *et al.*¹² found a moderate impact of electronic correlations with the EES being far less important than the previously calculated¹¹ ELS. Xu *et al.*²⁰ evaluated EES for the perfect hcp lattice and combined it with a separately calculated ELS term using the Mathiessen's rule. They obtained a significant reduction of the total conductivity and argued that the EES would be further enhanced if the large thermal disorder due to the motion of the ions close to (and above) the melting temperature were to be taken into account in its evaluation.

The questions on the relative impact of EES and its interplay with the ELS are also highly relevant if the main constituent of the inner core is the bcc iron phase.^{16–18} The bcc-phase has been pointed out to be significantly more correlated, compared to hcp-Fe, due to a van-Hove singularity in its electronic structure slowing down electrons.^{19,22,23} Dense bcc iron is expected to exist only at high temperatures close to melting; its stabilization is predicted to be induced by anharmonic ionic vibrations²⁴ or a complex "self-diffusion" mechanism.¹⁸ Very strong deviations from the perfect bcc crystalline order are thus

expected. Therefore, possible impact of these distortions on electronic correlations needs to be taken into account. Intuitively, one might expect the crystalline disorder to slow down the electrons further, which would enhance the effects of electronic correlations, as suggested by Xu *et al.* The impact of intertwined crystalline disorder and many-electron effects on transport has not been assessed in previous theoretical studies in iron at Earth's core conditions,^{12,20,25} though Hausoel *et al.* evaluated the strength of correlations in a thermally disordered face-centered cubic (fcc) phase of Ni at Earth's core conditions finding the impact of lattice vibrations on correlations insignificant.

In the present work we investigate these questions by considering electron transport in iron under conditions relevant to the inner core. We mainly focus on the bcc phase, where both the electronic correlations and complex non-harmonic lattice degrees of freedom are expected to play important role in accordance with previous studies.^{18,22–24,26} We describe this phase by applying the density functional + dynamical mean-field theory (DFT+DMFT) method^{27–29} to a set of Fe super-cells (SCs) randomly chosen from configurations produced by molecular dynamics (MD) simulations, as done earlier in Refs. 19 and 20. Our transport calculations thus include both the effects of the deformations of the lattice due to the thermal motion of ions as well as the electronic correlations (the latter are evaluated within the DMFT approximation). See more details on our approach to electronic structure and transport calculations in the Method section.

We find two main results: Firstly, the positional disorder does affect the electronic correlations but in contrast to expectations we find that their strength is suppressed. We rationalize this by the fact that the van Hove singularity present in perfect bcc-Fe^{23,30} is smoothed by thermal disorder, which reduces the EES. The total resistivity is to a large extent determined by the effects of thermal disorder and enhanced by less than one quarter by the EES. As the EES is insignificant, the Wiedemann-Franz law is obeyed to a higher precision than what is found for the undistorted lattice. Secondly, even with EES artificially increased above our calculated value its impact on the total resistivity is far less than expected on the basis of Matthiessen's rule. We derive a qualitative explanation of this surprising result that holds universally in the limit of strong disorder, i. e. in proximity to melting temperatures (and above).

As the thermal disorder wipes out the sharp characteristic features of the DOS one may actually expect a similar behaviour of the EES for the hcp, fcc and liquid phases. We verify the generality of our conclusions with explicit DFT+DMFT calculations of transport in the thermally disordered hcp phase, for which we obtain values of the total conductivity and EES contribution virtually coinciding with those for bcc. The relative insensitivity of the transport properties to both increase of the EES and particularities of the lattice structure thus

implies a robustly high conductivity in the presence of a strong EES also in other solid and liquid iron phases.

I. RESULTS

A. Electron-electron scattering effects on transport in presence of thermal disorder

We first present our key results on the conductivity of bcc-Fe at the inner core conditions. The resulting total electrical resistivity and thermal conductivity for this set that we evaluated for temperature $T = 5803$ K are shown in Fig. 1 (open triangles; the average over the SCs is shown with the bold star) together with results for the perfect bcc and hcp¹² lattices (for which the temperature dependence is also shown). The resistivity of perfect lattices is due to the EES term only; the temperature dependence in the case of bcc exhibits a rather slow non-Fermi-liquid²³ increase in contrast to the Fermi-liquid hcp phase.¹² The ELS starts contributing once lattice distortions are included. With the magnitude of the distortions predicted by our MD simulations the ELS is by far the dominating term, as one sees by comparing the total conductivities with purely ELS ones also shown in Fig. 1.

One may notice that the spread in the conductivities within the set is quite small thus showing little variation between different random configurations. Overall the value of the total bcc-Fe thermal conductivity averaged over all 8 distorted SCs in our set is equal to 220 W/(m·K) compared to 653 W/(m·K) for the EES only (perfect bcc lattice) and 275 W/(m·K) for the ELS only. For the electrical resistivity the corresponding values are $6.02 \cdot 10^{-5}$, $1.56 \cdot 10^{-5}$, and $5.82 \cdot 10^{-5}$ $\Omega \cdot \text{cm}$, respectively. By comparing the total conductivity κ with electron-lattice $\kappa_{\text{el-lat}}$ one infers that the EES reduces the thermal conductivity by about 20%; its impact on electrical resistivity is even smaller.

It is instructive to check the validity of the Wiedemann-Franz law $\kappa = L_0 \sigma T$, where $L_0 = 2.44 \times 10^{-8} \text{W}\Omega\text{K}^{-2}$ is the standard Lorenz number, by taking the ratios of thermal and electrical conductivity. For the perfect lattice we obtain $L = 1.62 \times 10^{-8} \text{W}\Omega\text{K}^{-2}$ whereas for the distorted one we obtain $L = 2.28 \times 10^{-8} \text{W}\Omega\text{K}^{-2}$. The former result deviates from the standard Lorenz number due to the frequency dependent inelastic scattering rate. The later result is close to L_0 . As pointed out above, thermal disorder provides the largest contribution to the overall scattering. This dominant contribution of thermal disorder, in contrast to the inelastic electron-electron scattering, influences the thermal and electrical conductivity equally resulting in an almost standard value for the Lorenz number.

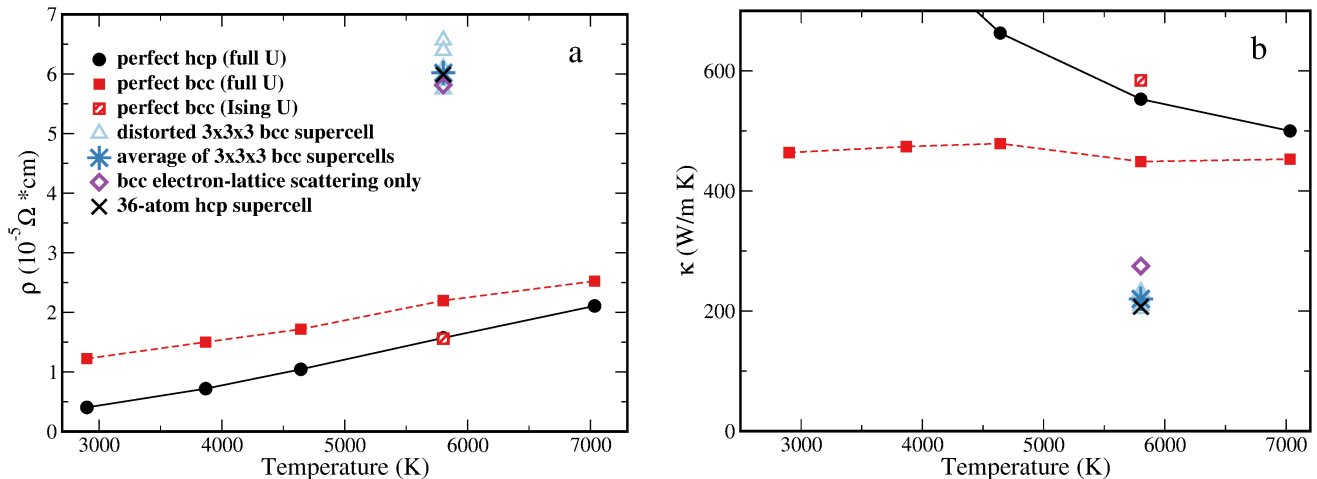


FIG. 1. a. The total resistivity of iron at Earth's core volume ($7 \text{ \AA}^3/\text{atom}$, density 13.2 g/cm^3) obtained by DFT+DMFT. The curves vs. temperature with filled circles/squares are for the perfect hcp¹² and bcc unit cells, respectively, calculated with the full rotationally invariant vertex. The rest of shown data is obtained using the density-density (Ising) vertex. The hashed red square is the perfect bcc result. In the case of perfect lattices the ELS term is absent and the resistivity is due to the EES term only. The empty triangles are for eight different distorted $3 \times 3 \times 3$ bcc supercells. The bold blue star is the average value over the distorted bcc supercells. The black cross is the average value over the representative 36-atoms hcp SC. The ELS resistivity calculated within DFT for bcc (purple empty diamond) is also shown. b. The total thermal conductivity of iron at Earth's core volume obtained by DFT+DMFT. The meaning of symbols is the same as for panel a.

B. Self-energy and spectral function

The electronic correlations, which are the origin of EES, are described in our framework by the local electronic self-energy. We have computed this quantity for a set of eight $2 \times 2 \times 2$ SCs with the fully self-consistent DFT+DMFT method (see Method section). In order to elucidate the effect of thermal disorder on electronic correlations one may compare the self-energy calculated in distorted SC with that in perfect lattices. Of particular relevance to transport is the low-frequency behavior of the imaginary part of the Matsubara³¹ self-energy $\text{Im}\Sigma(i\omega_n)$. The extrapolation of $|\text{Im}\Sigma|$ to low frequencies characterizes the electron scattering rate and the slope of the approach characterizes the electronic renormalization $m^*/m = [1 - d\text{Im}\Sigma(i\omega_n)/d(i\omega_n)]|_{\omega_n \rightarrow 0}$. Larger magnitude of $\text{Im}\Sigma(i\omega_n)$ thus points to stronger correlations. The calculated imaginary part of the Matsubara self-energies for different Fe $3d$ orbitals and atoms in the set of SCs is shown in Fig 2a together with those for the perfect bcc and hcp lattices.

One sees that thermal disorder significantly modifies the electronic self-energies. The self-energies at different positions differ and the largest differences are comparable to the value itself. One also sees that, unlike in the case of the perfect bcc structure, where there is a clear distinction between the more correlated non-Fermi liquid e_g and the less correlated Fermi-liquid t_{2g} self-energy, the self-energies of different atoms and orbitals quasi-uniformly span the full range of values. Therefore, thermal disorder is sufficiently large for the resulting self-energies not

to resemble those of the perfect bcc structure. (If the disorder were smaller, one would still resolve the t_{2g}/e_g blocks). The self-energy $\langle \Sigma \rangle$ averaged over all sites and SCs (and used, analytically continued to the real axis, Fig. 2b, for evaluating the conductivity in the $3 \times 3 \times 3$ SCs) is close to the bcc result for the less correlated t_{2g} orbital and to the Fermi-liquid self-energies of hcp-Fe. The more correlated bcc e_g result represents a rough upper bound. The average scattering rate (the imaginary part $\langle \text{Im}\Sigma(\omega) \rangle$) vs. ω exhibits a characteristic Fermi-liquid parabolic shape (Fig. 2b), with its value at the Fermi level, $\langle \text{Im}\Sigma(\omega = 0) \rangle = 84 \text{ meV}$, being close to the value of 90 meV previously obtained for hcp-Fe.¹² The thermal disorder thus reduces the electronic correlations compared to the perfectly crystalline bcc result.

In order to understand the origin of this effect, it is convenient also to look at the corresponding DFT+DMFT spectral function. Namely, the stronger correlations for the e_g orbital in the case of bcc structure occur due to the proximity to a van-Hove singularity.^{19,22,23,32} The $3d$ spectral function averaged over all sites in all 8 SCs is shown in Fig 2c and is compared to the one for the perfect bcc. One sees that the narrow peak of e_g states in the vicinity of $\omega = 0$ is almost completely smeared by lattice distortions. This smearing of the low-frequency peak in turn leads to weaker correlations. One thus has a counter-intuitive situation that the disorder actually leads to a suppression of electronic scattering at low energies.

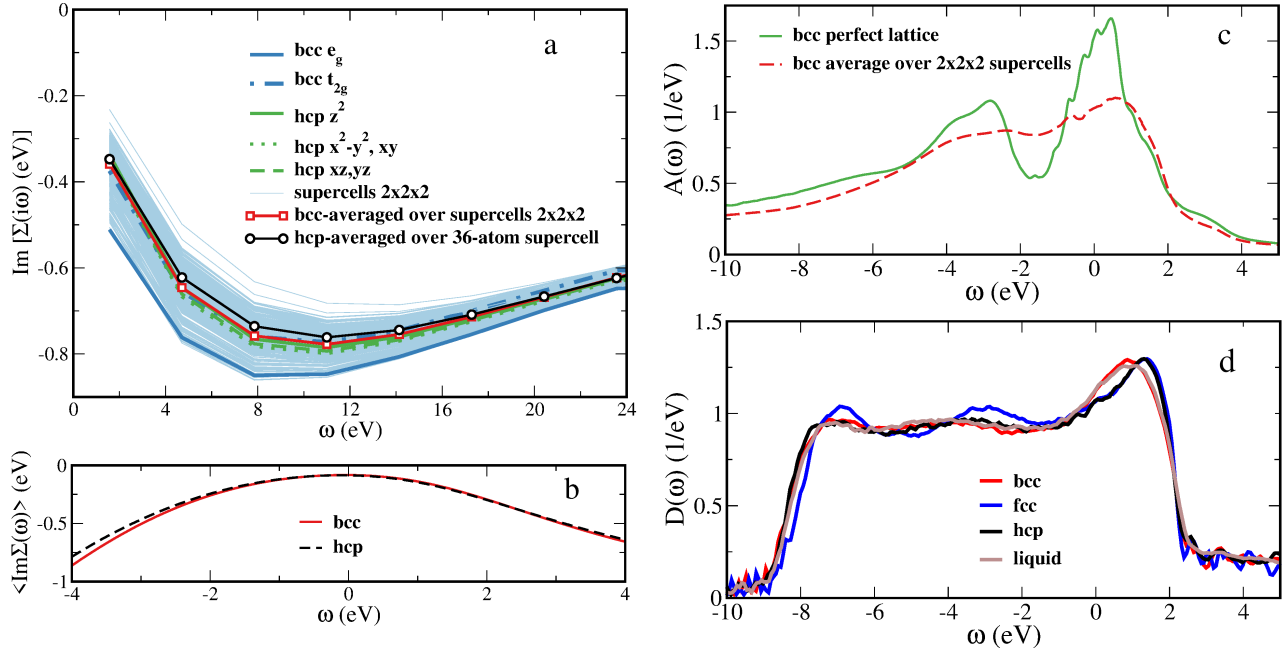


FIG. 2. a. The imaginary part of DMFT self-energy on the Matsubara grid for different atomic sites and orbitals of the set of $2 \times 2 \times 2$ bcc supercells (thin light blue curves). The average self-energy over all sites and orbitals of all bcc supercells (thick red line with squares) and the average self-energy over sites and orbitals of the hcp 36-atoms SC (black line with circles) are also shown. The blue and green curves are the self-energies for the non-degenerate orbitals in the perfect bcc and hcp lattices, respectively. b. The average DMFT bcc (red) and hcp (dashed black) self-energy in real frequency. c. The DMFT spectral function for the Fe $3d$ states averaged over all sites in the set of $2 \times 2 \times 2$ bcc supercells (red dashed line) compared to that for the perfect bcc lattice (solid green line). d. The DFT densities of states of the bcc, fcc, hcp and liquid iron at Earth's core density $7 \text{ \AA}^3/\text{atom}$ and $T = 6000 \text{ K}$ obtained by MD simulations.

C. Evolution of transport as a function of distortion

It is important to notice that whereas the electronic self-energies are actually suppressed when evaluated in the presence of thermal disorder, as shown above, the calculated resistivity is strongly increased implying that the increase must be attributed to the distortions.

In order to understand better the influence of distortions it is convenient to study the evolution of transport vs. distortion strength. To that end we chose a representative $2 \times 2 \times 2$ SC, for which the calculated thermal conductivity of $240 \text{ W}/(\text{m}\cdot\text{K})$ is close to the one obtained from the average over the whole $2 \times 2 \times 2$ set. The atomic coordinate \mathbf{R}_i of a given site i in this $2 \times 2 \times 2$ SC can be written as $\mathbf{R}_i = \mathbf{R}_i^0 + \tau_i$, where \mathbf{R}_i^0 denotes the position of the atom in the perfect $2 \times 2 \times 2$ SC and τ_i is the corresponding displacement in the distorted cell. Introducing a scaling parameter λ for the distortion, $\mathbf{R}_i^\lambda = \mathbf{R}_i^0 + \lambda \tau_i$, one can smoothly tune the distortion from the vanishing one $\lambda = 0$, to the actual distortion in the molecular dynamics simulation snapshot, $\lambda = 1$, and beyond (until the atomic spheres start to overlap, which occurs above $\lambda = 1.25$).

We performed full self-consistent DFT+DMFT calculations for a set of λ , the resulting electrical and thermal

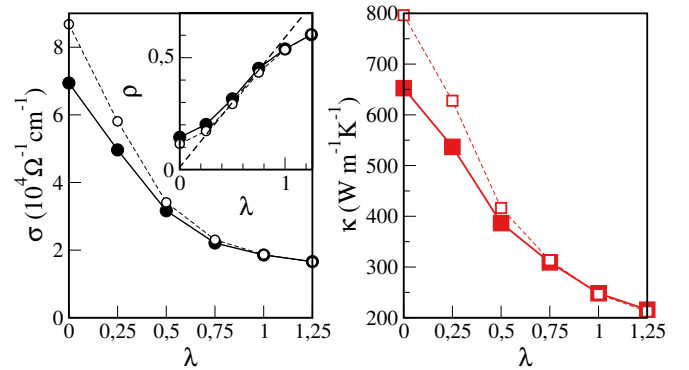


FIG. 3. The dependence of electrical (left panel) and thermal (right panel) conductivities on the degree of distortion λ (see text). The solid lines (full symbols) are calculated with full self-consistent DFT+DMFT, dashed lines (empty symbols) are obtained using the averaged self-energy (Σ) at full distortion $\lambda = 1$. The inset shows resistivity ρ and indicates the onset of saturation at large λ with deviation from linearity (dashed).

conductivities vs. λ are shown in Fig. 3. One can identify the regime of weak disorder with, in particular, a rather rapid decay of κ vs. $\lambda < 0.25$. By inserting the average self-energy (Σ) of fully distorted SCs instead of the one

calculated at a given λ one obtains a significantly larger conductivity at $\lambda = 0$ and a yet steeper decay. The difference in behavior of conductivities vs. $\lambda < 0.25$ for those two cases is due to the evolution of electronic self-energies upon increasing distortions. Namely, the distortions suppress the non-Fermi-liquid behavior of e_g orbitals (see Fig. 2) and reduce the overall magnitude of scattering $\sim |\text{Im}\Sigma(\omega)|$; this reduction of EES partially compensates the enhancement of ELS with λ .

The decrease of the conductivity becomes drastically slower for $\lambda > 0.5$. This saturation of conductivity seen in Fig. 3 and resistivity (inset) is related to the phenomenon of resistivity saturation that is known to occur in weakly correlated metals at elevated temperatures³³ and to play an important role for the transport in Fe.⁶ Namely, in weakly correlated metals the resistivity saturates at a so-called Mott-Ioffe-Regel value that corresponds to a scattering length equal to the minimal interatomic distance; this limit is $\sim 50\mu\Omega\text{cm}^{20}$ for Fe under Earth-core conditions. Notice that change in λ emulates change in temperature, as phonon displacement is proportional to temperature.

On the other hand, when electronic correlations become dominant the resistivity can grow further, which is called the bad-metal regime.³³ This is evidenced by the data in Fig. 4(b), where we artificially increased the strength of the EES, as discussed below. We stress that our approach correctly reproduces both the phenomenon of resistivity saturation and the bad-metal regime, whichever is applicable in the given case.

We notice also that for $\lambda > 0.5$ the evolution of transport vs. λ evaluated with $\langle\Sigma\rangle$ also becomes basically indistinguishable from that obtained with full calculations. Hence, at strong disorder the self-energy ceases to be sensitive to λ and saturates at average $\langle\Sigma\rangle$; this validates the use of $\langle\Sigma\rangle$ to evaluate transport in the strong-disorder regime.

D. Optical conductivity and interpretation of the results

To investigate the interplay between the thermal disorder and the EES further we also artificially tuned the strength of EES by multiplying the imaginary part of DMFT self-energy by a constant α and evaluated the transport for a fixed distorted lattice. Namely, we calculated the optical conductivity Eq. (8) as a function of the scale factor α , i.e. with the self-energy $\Sigma_\alpha(\omega) = \text{Re}\langle\Sigma(\omega)\rangle + \alpha\text{Im}\langle\Sigma(\omega)\rangle$ used for all orbitals and sites of a SC. Such a "cartoon" scaled self-energy, though not satisfying the exact Kramers-Kronig relations between $\text{Re}\Sigma(\omega)$ and $\text{Im}\Sigma(\omega)$, does capture main features of the strong EES regime in a Hund's system like iron: increasing strength of correlations resulting in a crossover to a non-Fermi-liquid behavior with the lifetime of states relatively far away from the Fermi level becoming short. Alternatively, uniformly scaling both the real and imag-

inary parts would respect the Kramers-Kronig relations, but in result one would apply a large coherent Fermi-liquid renormalization to $3d$ bands in a wide energy range. The latter is a physically incorrect representation of the strongly-correlated limit in iron.

A larger SC size is preferable in calculations with the scaled self-energy Σ_α in order to properly evaluate the DC-conductivity limit at small values of α . We thus chose a representative $3\times 3\times 3$ SC with the conductivities at $\alpha = 1$ very close to the average one (see Fig. 1). The resulting optical conductivity vs. α is displayed in Fig. 4.

The calculated optical conductivity is generally smooth and virtually constant at small $\omega \rightarrow 0$ due to a strong disorder suppressing the Drude peak coming from the intraband transitions in favor of low-lying interband transitions. At small $\alpha \leq 0.4$ the Drude peak is still present, due to insufficiency of the $3\times 3\times 3$ SC size to describe the electron-lattice scattering for very long-lived quasiparticle states. One may notice a rather slow decrease of conductivity vs. α ; with the EES increased by a factor of 40 $\sigma_1(0)$ is reduced by less than half of its initial value.

The Matthiessen's rule predicts the total (electrical or thermal) resistivity to be given by a sum due to separate scattering mechanisms; i.e. in the present case the total Matthiessen's rule thermal conductivity κ_M is given by $1/\kappa_M = 1/\kappa_{\text{el-lat}} + 1/\kappa_{\text{el-el}}$, where our calculated $\kappa_{\text{el-lat}} = 275\text{W}/(\text{m}\cdot\text{K})$. We calculated $\kappa_{\text{el-el}}$ as a function of α in the perfect bcc lattice by DFT+DMFT. The resulting relative deviation $\epsilon_M = \frac{\kappa - \kappa_M}{\kappa_M}$ of Matthiessen's rule conductivity with respect to the actual one (i.e. calculated with DFT+DMFT in the same distorted SCs and with $\text{Im}\langle\Sigma(\omega)\rangle$ scaled by α) is plotted in the inset of Fig. 4 as a function of α . One sees that the Matthiessen's rule is satisfied reasonably well at a small EES, but at the large EES limit the deviation becomes significant with the Matthiessen's rule underestimating the conductivity by about one third. Even the largest considered EES case that corresponds to $\alpha = 8$, for which $\kappa_{\text{el-el}} = 148\text{W}/(\text{m}\cdot\text{K})$, the calculated total conductivity is $\kappa = 125\text{W}/(\text{m}\cdot\text{K})$, while the corresponding $\kappa_M = 96\text{W}/(\text{m}\cdot\text{K})$ is markedly smaller.

In order to understand this effect we return to the expression for the DMFT conductivity (8). To simplify the discussion, it is convenient to neglect site/orbital dependence of the self-energy (which we argued above not to play an important role at the relevant conditions anyhow). Under this assumption the self energy has no momentum dependence and the DC conductivity can be written as

$$\sigma \propto \int d\omega \sum_k \sum_{\nu\nu'} |v_{k\nu\nu'}|^2 A_{k\nu} A_{k\nu'} (-df/d\omega). \quad (1)$$

The spectral function $A_{k\nu} = -1/\pi\text{Im}(\omega + \mu - \epsilon_{k\nu} - \Sigma)^{-1}$ can be further simplified by assuming that the self-energy is well described by a constant $\Sigma \sim -i\Delta$. The spectral functions hence take a Lorentzian form of width given by Δ . We observed that large disorder leads to a behavior that enables a further simplification of the expres-

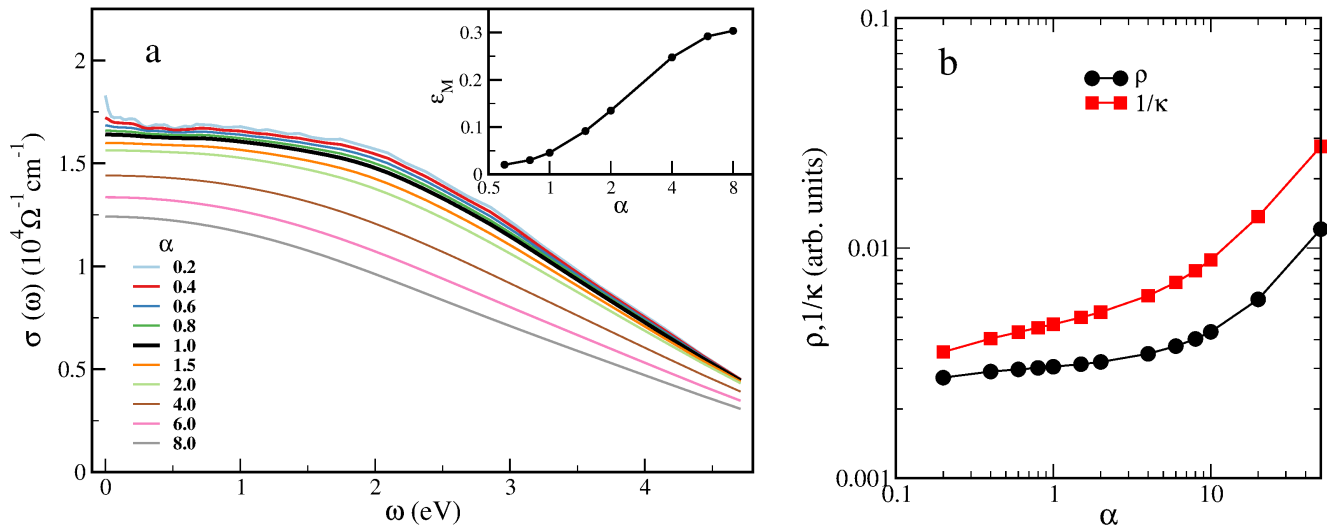


FIG. 4. a. The optical conductivity of a representative $3 \times 3 \times 3$ supercell vs. scale factor α applied to the imaginary part of DMFT self-energy (see text). The inset shows the relative deviation of calculated thermal conductivity from the Matthiessen's rule as a function of α . b. Calculated thermal and electrical conductivity as a function of α . Notice the slow dependence in the vicinity of $\alpha = 1$.

sion above: i) The eigen-energies become approximately equidistantly distributed, $\epsilon_{k\nu+1} - \epsilon_{k\nu} \approx C$, where C is a constant; (ii) The current matrix element $|v_{k\nu\nu'}|$ loses strong dependence on ν, ν' and essential physics can be reproduced by substituting it by a constant v^2 . Under these assumptions the conductivity simplifies to a form

$$\begin{aligned} \sigma &= \int d\omega v^2 \sum_k \sum_\nu A_{k\nu} \sum_{\nu'} A_{k\nu'} (-df/d\omega) \quad (2) \\ &= v^2 \int d\omega \left(\int d\epsilon A_\epsilon(\omega) \right)^2 (-df/d\omega), \end{aligned}$$

where in the last equality we replaced the summation over band-energies by a Riemann integral

$$\sum_\nu A_{k\nu} \rightarrow \frac{1}{\pi C} \int_{-W/2}^{W/2} d\epsilon \frac{\Delta}{(\omega + \mu - \epsilon)^2 + \Delta^2}, \quad (3)$$

where W is the bandwidth.

Now, when $W \gg \Delta$, the Riemann integral reduces to integration of a Lorentzian over range $(-\infty, \infty)$ and can be approximated by a constant. The resulting σ hence does not depend on Δ anymore. Only when one increases the electronic scattering above the full bandwidth ($\Delta \gg W$) a new regime occurs, where the integral (3) becomes $\propto W/\Delta$. In this regime the resistivity strongly ($\propto \Delta^2$) increases as a function of Δ . One sees a crossover to this regime in Fig. 4b at very large α . However, in the relevant range $\alpha \sim 1$ enhancement of Δ , while reducing the contribution of each individual $A_{k\nu}$, at the same time leads to the spectral functions further from Fermi energy contributing to the DC conductivity. This increase in the number of contributing ν “conduction channels” hence compensates for the loss of

conductivity due to a shorter electronic life-time. In result, the dependence of σ on Δ at $\alpha \sim 1$ is weak as seen in Fig. 4b. That is in contrast to the usual Drude behavior $\sigma \propto 1/\Delta$ occurring when the EES contribution (subsequently combined with ELS using the Matthiessen's rule) is calculated for the undistorted lattice.

II. DISCUSSION

The main results of our study α -Fe are thus: (1) EES is not increased but rather suppressed by thermal disorder, (2) the overall effect of EES on the transport properties in the presence of thermal disorder is small, lowering the thermal conductivity by about 20% but not more, (3) in the relevant regime the total conductivity exhibits markedly weaker dependence on the EES as compared to predictions of the simple Matthiessen's rule.

What are the implications of our analysis for the case of the hcp-phase, which is another candidate for the inner core's principal component, and for the outer core liquid phase? Should one expect a different behavior with stronger influence of EES from that found here? We show below that in fact this is not the case. The EES amplitude comes out to be very similar. In fact, the distinction between crystalline phases (as well as between them and the liquid phase) becomes smaller with increasing motion amplitude of the ions and peculiar features of their electronic structure are washed away. We compare the DFT densities of states obtained by averaging over MD configurations in Fig. 2d. Indeed, the difference between various iron crystalline phases as well as between them and liquid is quite insignificant, while it is striking in the case of perfect lattices at Earth's core density, see, e.g.,

Fig. 3 of Ref. 23 .

We verified the validity of these qualitative arguments by explicit calculations of the conductivity for a representative configuration of thermally disordered hcp Fe. We employed the same DFT+DMFT approach as in the case of bcc, see Method section for more details of these calculations. The electronic self-energy in the thermally disordered hcp phase is found to preserve its Fermi-liquid character;¹² the average hcp self-energy is hardly distinguishable from that of bcc, see Figs. 2a and b. The resulting values of electrical resistivity and thermal conductivity of hcp-Fe are $5.99 \cdot 10^{-5} \Omega \cdot \text{cm}$ and $207 \text{ W}/(\text{m} \cdot \text{K})$, respectively. As one sees (Fig. 1) they are very close to those for thermally disordered bcc. For the total (ELS+EES) conductivity of hcp-Fe we obtain $207 \text{ W}/(\text{m} \cdot \text{K})$, is higher than the previous theoretical values of $190 \text{ W}/(\text{m} \cdot \text{K})$ and $150 \text{ W}/(\text{m} \cdot \text{K})$ reported by Pourvskii *et al.*¹² and Xu *et al.*²⁰ Both Refs. 12 and 20 employed the Matthiessen's rule to evaluate the total thermal conductivity; as shown above this rule underestimates the conductivity. Moreover, Xu *et al.*²⁰ also employed a Boltzmann theory approach supplemented with a simple correction for the resistivity saturation to the ELS conductivity; their method underestimates the ELS conductivity as compared to our MD-based DMFT approach that naturally accounts for the saturation effect (see Fig. 3 and the discussion therein). Notice that the density of states of the perfect bcc and hcp iron phases are qualitatively different with the former featuring a peak at the Fermi level E_F due to the van Hove singularity, as discussed in Sec. I B, while the latter features a deep at E_F . However, once the thermal disorder is properly included the difference in both the electronic structure and conductivity almost disappears.

Finally, given a slow dependence of the total thermal conductivity on the magnitude of the EES (Fig. 4) in the disorder-dominated regime it is unlikely that electronic correlations would have a very important effect on the transport properties, even if the magnitude of EES turned to be somewhat larger than was found in the present work.

III. METHODS

Our DFT molecular dynamics were performed with the VASP code.³⁴ We used the projector augmented wave method^{34,35} to describe the interactions between the electrons and the ions, and expanded the single particle orbitals as linear combinations of plane waves (PW), including PW with maximum energies of 293 eV. The Brillouin zone was sampled using the (0.25, 0.25, 0.25) point only (in units of reciprocal lattice vectors). The time step was 1 fs and the temperature was controlled using a combination of Nosé³⁶ and Andersen³⁷ thermostats.

The DFT+DMFT calculations were performed using a full-potential self-consistent in the charge density approach^{38,39} based on the Wien-2k code⁴⁰ and TRIQS

library.^{41,42} These calculations were carried out for a set of 8 distorted $2 \times 2 \times 2$ supercells (SCs) with the volume $7 \text{ \AA}^3/\text{atom}$ randomly drawn from configurations produced by DFT molecular dynamics simulations. We employed the same values of the Coulomb interaction parameters $U = 5.0 \text{ eV}$, $J_H = 0.93 \text{ eV}$ as in the previous study of the conductivity in perfect hcp¹² and the energy window $[-12.2 \text{ eV}, 4.0 \text{ eV}]$ around the Fermi level for the Kohn-Sham states used to construct Wannier orbitals representing Fe $3d$ states. The DMFT impurity problem was solved by the hybridization-expansion quantum Monte Carlo impurity solver.⁴³ The density-density approximation was employed for the interaction vertex (which leads to an underestimation of the EES thermal resistivity by 30 to 40% for the perfect iron phases, see Fig. 1 and ref. 21) and the non-diagonal elements of the bath Green's function were neglected in the impurity problem.

Each SC was first converged by about 20 fully self-consistent DFT+DMFT iterations with subsequent 10 additional DMFT cycles using the converged Kohn-Sham Hamiltonian. Each Monte Carlo run employed 10^{10} Monte-Carlo moves and 200 moves/measurement. Subsequently, 25 additional runs were carried out starting from the same converged value of the DMFT bath Green's function and resetting the random sequence. Such full DFT+DMFT run for a single 16-atom cell typically took about 7 days of calculation time on a 64-core cluster. The self-energies thus obtained were then averaged to obtain the final high-precision DMFT self-energy, which was analytically continued using the Maximum Entropy method⁴⁴ to the real-energy axis. The conductivity along the [100] direction was calculated within the Kubo linear-response formalism. Namely, the electrical and thermal conductivity read

$$\sigma_{\alpha\alpha'} = \frac{e^2}{k_B T} K_{\alpha\alpha'}^0, \quad (4)$$

$$\kappa_{\alpha\alpha'} = k_B \left[K_{\alpha\alpha'}^2 - \frac{(K_{\alpha\alpha'}^1)^2}{K_{\alpha\alpha'}^0} \right], \quad (5)$$

where α is the direction (x , y , or z), k_B is the Boltzmann constant.

The kinetic coefficients $K_{\alpha\alpha'}^n$ read

$$K_{\alpha\alpha'}^n = 2\pi\hbar \int d\omega (\beta\omega)^n f(\omega) f(-\omega) \Gamma^{\alpha\alpha'}(\omega, \omega), \quad (6)$$

where 2 is the spin factor, $f(\omega)$ is the Fermi function, and the transport distribution $\Gamma^{\alpha\alpha'}$ is given by

$$\Gamma^{\alpha\alpha'}(\omega_1, \omega_2) = \frac{1}{V} \sum_{\mathbf{k}} \text{Tr} \left(v^\alpha(\mathbf{k}) A(\mathbf{k}, \omega_1) v^{\alpha'}(\mathbf{k}) A(\mathbf{k}, \omega_2) \right), \quad (7)$$

where V is the unit cell volume, $A(\mathbf{k}, \omega)$ is the DMFT spectral function and $v^\alpha(\mathbf{k})$ is the velocity, see ref. 42.

The optical conductivity is evaluated from the transport distribution as follows:

$$\sigma_{\alpha\alpha'}(\Omega) = 2\pi e^2 \hbar \int d\omega \Gamma^{\alpha\alpha'}(\omega + \Omega/2, \omega - \Omega/2) \frac{f(\omega - \Omega/2) - f(\omega + \Omega/2)}{\Omega} \quad (8)$$

Without the additional EES contribution evaluated by DMFT our approach would reduce to the conventional Kubo-Greenwood DFT formalism routinely used to evaluate the ELS contribution to the resistivity.^{11,45} The present approach thus additionally takes the EES into account.

The total thermal conductivity thus calculated and averaged over all 8 distorted $2 \times 2 \times 2$ SCs is equal to 245 W/(m·K). However, the 16-atom $2 \times 2 \times 2$ SC is not sufficient for a precise evaluation of the conductivity. As shown in Supplementary Information Fig. 2 one needs at least $3 \times 3 \times 3$ 54-atoms SCs to reach the convergence for the ELS conductivity. Full DFT+DMFT calculations are too time-consuming for these 54-atoms supercells. Instead a randomly chosen set of eight $3 \times 3 \times 3$ supercells was drawn from our MD simulations and converged in DFT. The average self-energy $\langle \Sigma(i\omega_n) \rangle$ previously obtained for the $2 \times 2 \times 2$ set (the blue curve in Fig. 2a) was subsequently inserted at each site together with the average double-counting term. Once the chemical potential was found, the conductivity was calculated using $\langle \Sigma(i\omega_n) \rangle$ analytically continued to real frequencies (Fig. 2b). This approach is based on the observation that the conductivity becomes insensitive to the site and orbital dependence of self-energy at the realistic distortion levels, see Fig. 3 in Sec. IC and the discussion therein. We also benchmarked this procedure on the $2 \times 2 \times 2$ set; thus calculated conductivities are in a good agreement with the full calculations, with the resulting average $\kappa = 232$ W/(m·K) compared to 245 W/(m·K) for full calculation in which the site and orbital depen-

dence is retained. The resulting total thermal conductivity evaluated with $3 \times 3 \times 3$ SCs and shown in Fig. 1, $\kappa = 220$ W/(m·K), is only slightly reduced compared to the magnitude obtained with the $2 \times 2 \times 2$ SCs (see Fig. 1 in Supplementary Information). Whereas the size of our SCs is insufficient to ensure dynamic stability of the bcc structure – a tour de force with 1024 atoms was needed in Belonoshko *et. al.*¹⁸ – the choice of the unit cell shape constrains the dynamics of ions to those representative of the thermodynamic limit, especially for the integrated quantities such as conductivity of interest to our work.

We applied the same framework to evaluate the conductivity in the hcp phase. To reduce the computational effort in this case we made use of the fact that the conductivity varies little between different SCs, as one sees on the example of bcc (Fig. 1). Hence, we chose a single representative 36-atom hcp SC ($3 \times 3 \times 2$ in crystallographic unit cells with $c/a = 1.6$ and volume $7 \text{ \AA}^3/\text{atom}$) from a set randomly drawn from our MD simulations. The value of calculated ELS conductivity for the chosen SC was the closest to the average over this set of 15 SC configurations. For that 36-atom SC we performed the same full DFT+DMFT calculation as described above for the set of $2 \times 2 \times 2$ bcc SCs. Parameters of this calculation (the values of U , J_H , the energy window for Wannier construction, number of DFT+DMFT iterations and quantum Monte Carlo cycles) were the same as for the bcc case.

For the sake of comparison the ELS contribution was also computed separately using the DFT-based framework of refs. 11 and 45. These DFT calculations of the ELS-only electrical and thermal conductivities were performed via the Kubo-Greenwood and the Chester-Thellung-Kubo-Greenwood⁴⁶ formula, respectively, as implemented in VASP.⁴⁷ We employed settings similar to those employed in,¹¹ by averaging over 72 statistically independent configurations on cells including between 16 and 250 atoms.

¹ B. Buffett, “Geomagnetism under scrutiny,” *Nature* **485**, 319–320 (2012).

² U. R. Christensen and J. Aubert, “Scaling properties of convection-driven dynamos in rotating spherical shells and application to planetary magnetic fields,” *Geophysical Journal International* **166**, 97–114 (2006).

³ F. Stacey and D. Loper, “A revised estimate of the conductivity of iron alloy at high pressure and implications for the core energy balance,” *Physics of the Earth and Planetary Interiors* **161**, 13–18 (2007).

⁴ P. Olson, “The new core paradox,” *Science* **342**, 431–432 (2013).

⁵ N. de Koker, G. Steinle-Neumann, and V. Vlček, “Electrical resistivity and thermal conductivity of liquid Fe alloys at high P and T, and heat flux in Earth’s core,” *Proc. Natl. Acad. Sci. U. S. A.* **109**, 4070–3 (2012).

⁶ M. Pozzo, C. Davies, D. Gubbins, and D. Alfè, “Thermal

and electrical conductivity of iron at Earth’s core conditions,” *Nature* **485**, 355–358 (2012).

⁷ R. K. Bono, J. A. Tarduno, F. Nimmo, and R. D. Cottrell, “Young inner core inferred from ediacaran ultra-low geomagnetic field intensity,” *Nature Geoscience* **12**, 143 (2019).

⁸ B. Romanowicz, X.-D. Li, and J. Durek, “Anisotropy in the inner core: Could it be due to low-order convection?” *Science* **274**, 963–966 (1996).

⁹ B. A. Buffett, “Onset and orientation of convection in the inner core,” *Geophysical Journal International* **179**, 711–719 (2009).

¹⁰ M. Monnereau, M. Calvet, L. Margerin, and A. Souriau, “Lopsided growth of Earth’s inner core,” *Science* **328**, 1014–1017 (2010).

¹¹ M. Pozzo, C. Davies, D. Gubbins, and D. Alfè, “Thermal and electrical conductivity of solid iron and iron-silicon

- mixtures at Earth's core conditions," *Earth and Planetary Science Letters* **393**, 159 – 164 (2014).
- ¹² L. V. Pourovskii, J. Mravlje, A. Georges, S. I. Simak, and I. A. Abrikosov, "Electron-electron scattering and thermal conductivity of ϵ -iron at Earth's core conditions," *New Journal of Physics* **19**, 073022 (2017).
 - ¹³ K. Ohta, Y. Kuwayama, K. Hirose, K. Shimizu, and Y. Ohishi, "Experimental determination of the electrical resistivity of iron at Earth's core conditions," *Nature* **534**, 95 (2016).
 - ¹⁴ Z. Konôpková, R. S. McWilliams, N. Gómez-Prez, and A. F. Goncharov, "Direct measurement of thermal conductivity in solid iron at planetary core conditions," *Nature* **534**, 99 (2016).
 - ¹⁵ Q. Williams, "The thermal conductivity of Earth's core: A key geophysical parameter's constraints and uncertainties," *Annual Review of Earth and Planetary Sciences* **46**, 47–66 (2018).
 - ¹⁶ L. Dubrovinsky, N. Dubrovinskaia, O. Narygina, I. Kantor, A. Kuznetsov, V. B. Prakapenka, L. Vitos, B. Johansson, A. S. Mikhaylushkin, S. I. Simak, and I. A. Abrikosov, "Body-centered cubic iron-nickel alloy in Earth's core," *Science* **316**, 1880–1883 (2007).
 - ¹⁷ R. Hrubiak, Y. Meng, and G. Shen, "Experimental evidence of a body centered cubic iron at the Earth's core condition," (2018), arXiv:1804.05109.
 - ¹⁸ A. B. Belonoshko, T. Lukinov, J. Fu, J. Zhao, S. Davis, and S. I. Simak, "Stabilization of body-centred cubic iron under inner-core conditions," *Nature Geoscience* **10**, 312–316 (2017).
 - ¹⁹ A. Hausoel, M. Karolak, E. Sasioglu, A. Lichtenstein, K. Held, A. Katanin, A. Toschi, and G. Sangiovanni, "Local magnetic moments in iron and nickel at ambient and Earth's core conditions," *Nature Communications* **8** (2017), 10.1038/ncomms16062.
 - ²⁰ J. Xu, P. Zhang, K. Haule, J. Minar, S. Wimmer, H. Ebert, and R. E. Cohen, "Thermal conductivity and electrical resistivity of solid iron at Earth's core conditions from first principles," *Phys. Rev. Lett.* **121**, 096601 (2018).
 - ²¹ L. V. Pourovskii, "Electronic correlations in dense iron: from moderate pressure to Earth's core conditions," *Journal of Physics: Condensed Matter* **31**, 373001 (2019).
 - ²² S. V. Vonsovsky, M. I. Katsnelson, and A. V. Trefilov, "Localized and itinerant behavior of electrons in metals," *Phys. Met. Metallogr.*, 247 (1993).
 - ²³ L. V. Pourovskii, T. Miyake, S. I. Simak, A. V. Ruban, L. Dubrovinsky, and I. A. Abrikosov, "Electronic properties and magnetism of iron at the Earth's inner core conditions," *Phys. Rev. B* **87**, 115130 (2013).
 - ²⁴ L. Vocadlo, D. Alfè, M. Gillan, I. Wood, J. Brodholt, and G. Price, "Possible thermal and chemical stabilization of body-centred-cubic iron in the Earth's core," *Nature* **424**, 536–539 (2003).
 - ²⁵ V. Drchal, J. Kudrnovský, D. Wagenknecht, I. Turek, and S. Khmelevskiy, "Transport properties of iron at Earth's core conditions: The effect of spin disorder," *Phys. Rev. B* **96**, 024432 (2017).
 - ²⁶ A. A. Katanin, A. I. Poteryaev, A. V. Efremov, A. O. Shorikov, S. L. Skornyakov, M. A. Korotin, and V. I. Anisimov, "Orbital-selective formation of local moments in α -iron: First-principles route to an effective model," *Phys. Rev. B*, 045117 (2010).
 - ²⁷ A. Georges, G. Kotliar, W. Krauth, and M. J. Rozenberg, "Dynamical mean-field theory of strongly correlated fermion systems and the limit of infinite dimensions," *Rev. Mod. Phys.* **68**, 13–125 (1996).
 - ²⁸ V. I. Anisimov, A. I. Poteryaev, M. A. Korotin, A. O. Anokhin, and G. Kotliar, "First-principles calculations of the electronic structure and spectra of strongly correlated systems: dynamical mean-field theory," *Journal of Physics: Condensed Matter* **9**, 7359 (1997).
 - ²⁹ G. Kotliar, S. Y. Savrasov, K. Haule, V. S. Oudovenko, O. Parcollet, and C. A. Marianetti, "Electronic structure calculations with dynamical mean-field theory," *Rev. Mod. Phys.* **78**, 865–951 (2006).
 - ³⁰ R. Maglic, "Van hove singularity in the iron density of states," *Phys. Rev. Lett.* **31**, 546–548 (1973).
 - ³¹ G. D. Mahan, *Many Particle Physics, Third Edition* (Plenum, New York, 2000).
 - ³² J. Mravlje, M. Aichhorn, T. Miyake, K. Haule, G. Kotliar, and A. Georges, "Coherence-incoherence crossover and the mass-renormalization puzzles in Sr_2RuO_4 ," *Phys. Rev. Lett.* **106**, 096401 (2011).
 - ³³ O. Gunnarsson, M. Calandra, and J. E. Han, "Colloquium: Saturation of electrical resistivity," *Rev. Mod. Phys.* **75**, 1085–1099 (2003).
 - ³⁴ G. Kresse and D. Joubert, "From ultrasoft pseudopotentials to the projector augmented-wave method," *Phys. Rev. B* **59**, 1758–1775 (1999).
 - ³⁵ P. E. Blöchl, "Projector augmented-wave method," *Phys. Rev. B* **50**, 17953–17979 (1994).
 - ³⁶ S. Nosé, "A molecular dynamics method for simulations in the canonical ensemble," *Molecular Physics* **52**, 255–268 (1984).
 - ³⁷ H. C. Andersen, "Molecular dynamics simulations at constant pressure and/or temperature," *The Journal of Chemical Physics* **72**, 2384–2393 (1980).
 - ³⁸ M. Aichhorn, L. Pourovskii, V. Vildosola, M. Ferrero, O. Parcollet, T. Miyake, A. Georges, and S. Biermann, "Dynamical mean-field theory within an augmented plane-wave framework: Assessing electronic correlations in the iron pnictide LaFeAsO ," *Phys. Rev. B* **80**, 085101 (2009).
 - ³⁹ M. Aichhorn, L. Pourovskii, and A. Georges, "Importance of electronic correlations for structural and magnetic properties of the iron pnictide superconductor LaFeAsO ," *Phys. Rev. B* **84**, 054529 (2011).
 - ⁴⁰ P. Blaha, K. Schwarz, G. Madsen, D. Kvasnicka, and J. Luitz, *WIEN2k, An augmented Plane Wave + Local Orbitals Program for Calculating Crystal Properties* (Techn. Universität Wien, Austria, ISBN 3-9501031-1-2., 2001).
 - ⁴¹ O. Parcollet, M. Ferrero, T. Ayal, H. Hafermann, I. Krivenko, L. Messio, and P. Seth, "TRIQS: A toolbox for research on interacting quantum systems," *Computer Physics Communications* **196**, 398–415 (2015).
 - ⁴² M. Aichhorn, L. Pourovskii, P. Seth, V. Vildosola, M. Zingl, O. E. Peil, X. Deng, J. Mravlje, G. J. Krabberger, C. Martins, M. Ferrero, and O. Parcollet, "TRIQS/DFTTools: A TRIQS application for ab initio calculations of correlated materials," *Computer Physics Communications* **204**, 200 – 208 (2016).
 - ⁴³ E. Gull, A. J. Millis, A. I. Lichtenstein, A. N. Rubtsov, M. Troyer, and P. Werner, "Continuous-time monte carlo methods for quantum impurity models," *Rev. Mod. Phys.* **83**, 349–404 (2011).
 - ⁴⁴ K. S. D. Beach, "Identifying the maximum entropy method as a special limit of stochastic analytic continuation," *Cond-mat/0403055*.
 - ⁴⁵ C. Davies, M. Pozzo, D. Gubbins, and D. Alfè, "Con-

straints from material properties on the dynamics and evolution of Earth’s core,” *Nature Geoscience* **8**, 678–685 (2015).

- ⁴⁶ G. V. Chester and A. Thellung, “The law of Wiedemann and Franz,” *Proceedings of the Physical Society* **77**, 1005–1013 (1961).
- ⁴⁷ M. P. Desjarlais, J. D. Kress, and L. A. Collins, “Electrical conductivity for warm, dense aluminum plasmas and liquids,” *Phys. Rev. E* **66**, 025401 (2002).

IV. ACKNOWLEDGMENTS

We are thankful to I. A. Abrikosov and S. I. Simak for valuable discussions and critical reading of the manuscript. Useful discussions with M. Ferrero and J. Vučičević are also acknowledged. L. P. acknowledges

support of the European Research Council grant ERC-319286-QMAC as well as computational resources of the Swedish National Infrastructure for Computing (SNIC) at the National Supercomputer Centre (NSC). L. P. is grateful to the computer team at CPHT for support. J.M. acknowledges support by Program P1-0044 of Slovenian Research Agency. D. A. and M. P. acknowledge support from the Natural Environment Research Council (NERC) Grants No. NE/ M000990/1 and No. NE/R000425/1. The DFT calculations are performed on the Monsoon2 system, a collaborative facility supplied under the Joint Weather and Climate Research Programme, a strategic partnership between the UK Met Office and NERC. Calculations are also performed at University College London Research Computing on the Materials and Molecular Modelling hub Grant No. EP/P020194/1 and on the Oak Ridge Leadership Computing Facility (Contract No. DE-AC05-00OR22725).

Supplementary information for "Electronic correlations and transport in iron at Earth's core conditions"

by L. V. Pourovskii, J. Mravlje, M. Pozzo, and D. Alfè

V. INFLUENCE OF THE SUPERCELL SIZE

In Fig. S1 we compare the thermal conductivity computed using the $2 \times 2 \times 2$ and $3 \times 3 \times 3$ distorted SCs using the average DMFT self-energy $\langle \Sigma \rangle$ (Fig. 2 of the main text). One may see that the magnitude of conductivity a little bit (by about 6%) decreases with the increasing SC size.

The test calculations for the perfect $2 \times 2 \times 2$ and $3 \times 3 \times 3$ SCs are also shown in the same figure; they are higher than those obtained for the perfect $2 \times 2 \times 2$ in real DFT+DMFT calculations (the red hashed square in Fig. 1b). The reason is, of course, that the correlations are reduced by lattice distortions as explained in the main text, see Figs. 2 and 3 of the main text and the discussion therein.

In Fig. S2 we show the ELS optical conductivity $\sigma_{\text{el-lat}}$ as well as the ELS frequency dependent thermal conductivity $\kappa_{\text{el-lat}}(\omega)$ calculated within DFT by the method of ref. 11 vs. the size of simulation SCs. The DC conductivity is obtained by taking the $\omega \rightarrow 0$ limit. One sees that the result with $3 \times 3 \times 3$ SCs is very close to that for the largest considered SC ($5 \times 5 \times 5$), while the one obtained with $2 \times 2 \times 2$ SCs still deviates from it and exhibits significant noise.

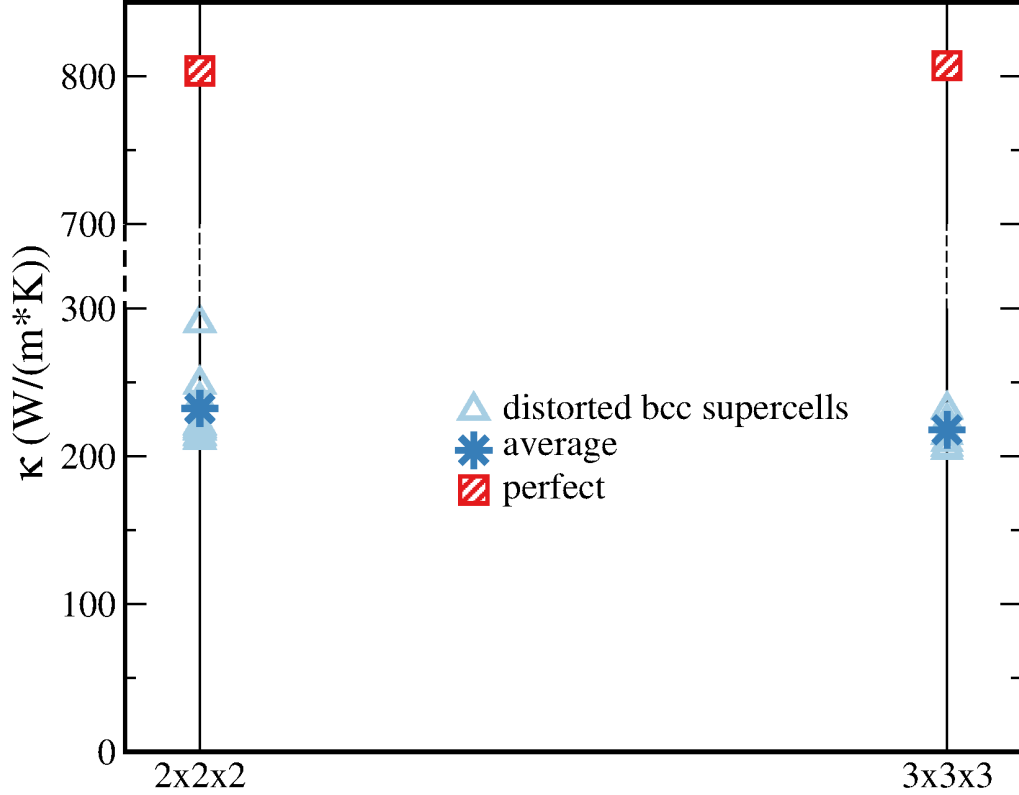


FIG. S1. The thermal conductivities for the sets of $2 \times 2 \times 2$ and $3 \times 3 \times 3$ supercells obtained with average Σ and double-counting inserted to their converged DFT band-structures as described in the text. The meaning of symbols is the same as in Fig. 1 of the main text

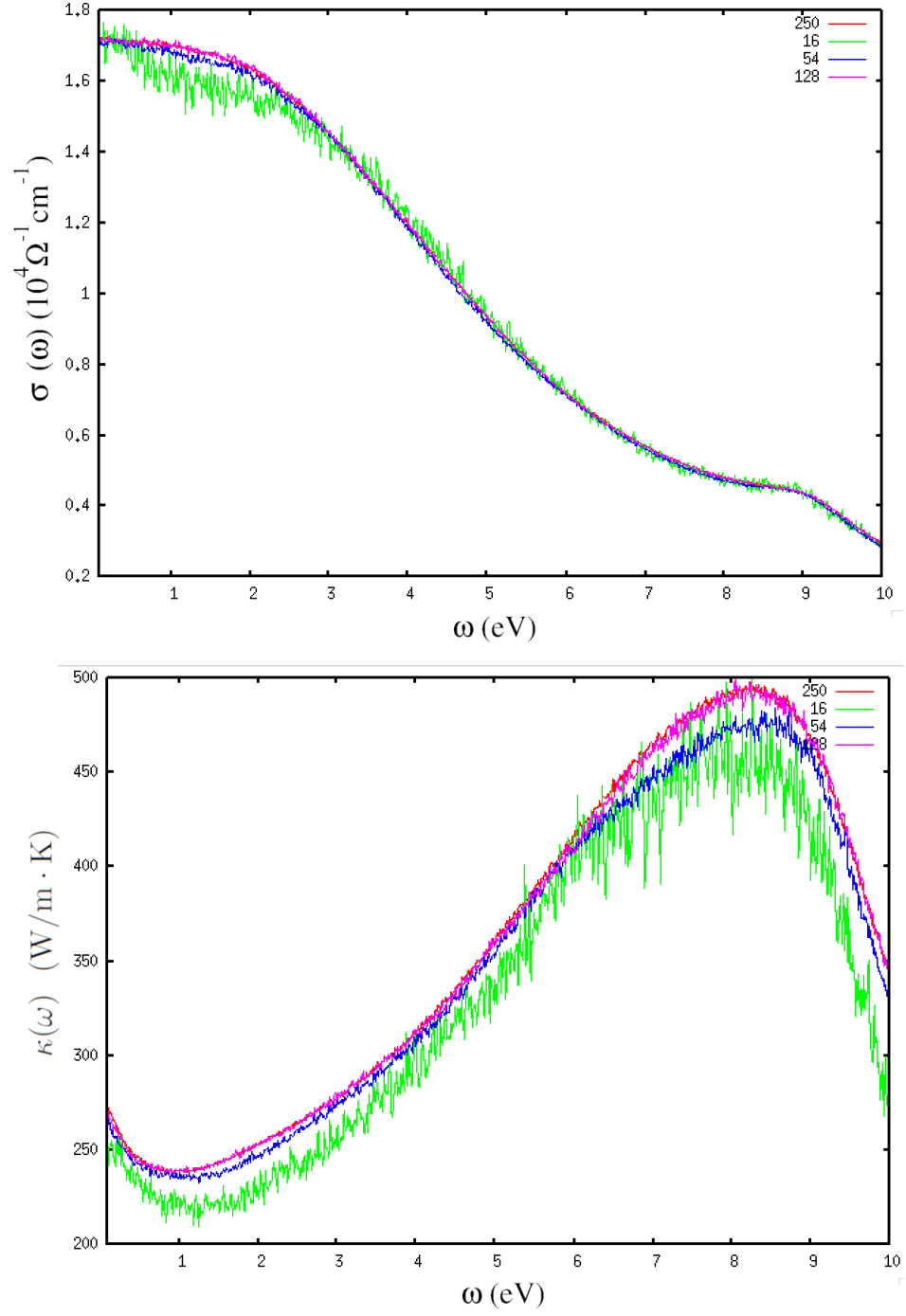


FIG. S2. The ELS optical conductivity (upper panel) and frequency-dependent thermal conductivity (lower panel) calculated within DFT using SCs of different sizes. The DC conductivity is obtained by taking the $\omega \rightarrow 0$ limit. One sees that the values obtained using the $3 \times 3 \times 3$ 54-atoms SCs are very close to final results with $5 \times 5 \times 5$ 125-atoms SCs.